This is a repository copy of *Analytical and experimental study on the seismic performance of cold-formed steel frames*.

Version: Accepted Version

Analytical and Experimental Study on the Seismic Performance of Cold-Formed Steel Frames

Seyed Mohammad Mojtabaei[1,*], Mohammad Zaman Kabir[2], Iman Hajirasouliha[1], Mina Kargar[2]

Department of Civil and Structural Engineering, University of Sheffield, Sheffield, UK

Department of Civil and Environmental Engineering, Amirkabir university of Technology, Tehran, Iran

* Corresponding author, E-mail: smmojtabaei1@sheffield.ac.uk

A B S T R A C T

This study aims to investigate the seismic performance of an innovative cold-formed steel (CFS) moment-resisting frame experimentally and analytically. A half-scale CFS moment-resisting portal frame was tested under static monotonic loading until failure. The frame consisted of two box-shaped columns (face-to-face channels connected with inside plates), a back-to-back lipped channel beam section and fully moment-resisting CFS bolted connections. During experimental tests, damage mostly concentrated at the top and bottom of the CFS columns due to the web crippling of the channels close to the connections, while no fracture or obvious slippage was observed at the connection zones. A detailed Finite Element (FE) model was developed using ABAQUS by taking into account the material non-linearity and geometrical imperfections. The lateral load-displacement behaviour, ultimate strength and failure modes predicted by the model were in very good agreement with the experimental results. The validated FE model was then used to assess the effects of key design parameters on the lateral load capacity, ultimate displacement, energy dissipation, ductility, and ductility reduction factor of the frame. It is shown that the proposed system can provide good seismic performance subjected to the appropriate design of the main structural elements. Increasing the axial load ratio of the columns by 50% resulted in 26%, 62%, and 50% decrease in the ultimate lateral load, energy dissipation capacity, and ductility ratio of the CFS frame,

respectively. However, the energy dissipation capacity and the ductility ratio of the proposed system increased significantly by increasing the width-to-thickness ratio of the columns.

Keywords: Cold-Formed Steel (CFS); Moment-Resisting Frames (MRF); Monotonic Loading; Energy Dissipation; Ductility

1 INTRODUCTION

Cold-formed steel (CFS) structural elements have seen a dramatic expansion in the range of applications over the past decade. CFS systems are currently used in structural, mechanical and aeronautical engineering. Compared to their hot-rolled counterparts, CFS members are often more economical and efficient due to their light weight, ease and speed of construction and a greater flexibility in manufacturing. However, the inherently low buckling resistance of thin sections results in relatively low strength and ductility in CFS structural elements, which may limit their performance under extreme loading events such as strong earthquakes. While the seismic performance of CFS structures has been previously investigated [1-5], majority of these studies have focused on the behaviour of shear wall panels as the main lateral load-bearing system. However, using moment-resisting CFS frames can reduce the reliance on the fixed shear wall panels and therefore provide higher flexibility for space planning (e.g. opening sizes and proportions) and future alterations. On the other hand, compared to shear wall systems, using moment-resisting CFS frames can potentially improve the energy dissipation capacity and the seismic performance of the CFS structures under strong earthquakes.

The structural performance of moment-resisting connections (named eaves and apex joints) with different bolt group sizes were investigated by Lim et al [6]. It was shown experimentally and numerically that the strength of web bolted moment resisting connections between cold-formed steel channels can be controlled by the length of the bolt groups. In

2

addition, the Direct Strength Method (DSM) adopted in North American design specifications [7], was further developed to predict the moment capacity of the connections with short and long bolt group length [8]. Sato and Uang [9] showed that the ductility capacity of CFS special bolted-moment frames defined by AISI S110 standard [10], can be improved through bolt slippage and bearing in bolted beam-to-column moment connections. However, it should be noted that AISI S110 [10] standard has now been supressed by AISI S100 [7].

Several studies have also investigated the seismic performance of bolted-moment connections using gusset plates [11-14], where the experimental results are used to validate different modelling techniques (e.g. detailed FE modelling, equivalent spring elements and internal force distributions) for prediction of stiffness and strength of the connections. It should be noted that based on the current AISI S400 standard [15], CFS bolted moment frame systems are expected to withstand inelastic friction and bearing deformation at the bolted-beam to column connections. The required strength of beams and columns in the CFS moment resisting frame system shall be determined from the expected moment developed at the bolted connection, using the column shear corresponding to the slip strength of the bolt group and the connection bearing component of column shear corresponding to the design storey drift.

Lim et al. [5] proposed a simplified beam element to model the structural behaviour of CFS portal frames and compared the FE results with those of full scale laboratory tests. It was shown that the deflection due to bolt-hole elongation has the most significant contribution to the total beam deflection. In another study, Sabbagh et al. [16] performed an experimental investigation to study the performance of two full scale one-storey frames made of cold-formed steel members under gravity and lateral cyclic loads. The results of their study in general indicate that CFS moment-resisting frames exhibit good seismic performance subjected to the appropriate details for the main structural elements.

In general, CFS moment-resisting frames investigated in the aforementioned studies provided a better ductility and energy dissipation capacity compared to conventional CFS shear wall panels. However, more studies are required to investigate the non-linear seismic performance of CFS moment-resisting frames using different types of connections and design parameters. In this paper, a CFS moment-resisting frame with box-shaped columns and back-to-back beam channels is laterally pushed monotonically until failure. Two different types of connections are used in this research (i): column-to-base connection fabricated with hot-rolled angle cleats bolted to the CFS column and base, (ii): beam-to-column connection assembled by gusset plates connected to both beam and column elements by using bolts. The failure mode of the tested moment-resisting CFS frame is identified and the structural behaviour of the frame is described step-by-step using a lateral load-displacement curve. A detailed FE model is developed by considering material nonlinearity, geometrical imperfections and accurate behaviour of the bolts. The results are then validated against the experimental response of the frame. Finally, a comprehensive parametric study is carried out to investigate the lateral load capacity, ultimate displacement, energy dissipation capacity, ductility, and ductility reduction factor of the CFS frames with different axial load levels and width-to-thickness ratios of the columns. The results are used to assess the adequacy of the proposed system is seismic regions.

2 EXPERIMENTAL STUDY

### 2.1 Specimen description and preparation

The aim of the experimental program in this study was to provide information on the seismic performance of an innovative CFS moment-resisting frame system by focusing on the lateral load-displacement behaviour and the failure modes.

The CFS moment-resisting frame was a half-scale representative of a moment-resisting frame with the height and the span length of 3000 mm (see

(c) A-A. Beam section.   (d) Column-to-base connection.

Fig. 1(a)). The cross-sectional dimensions and plate thicknesses were scaled so that the lateral stiffness of the scaled frame remains similar to the original frame. The CFS sections were formed by a press brake machine using galvanized steel sheets. However, it should be noted that generally cold-formed structural sections are manufactured by rolling process, causing residual stress and strain hardening of the material especially in the corner zones. The columns were built-up box-shaped sections consisting of face-to-face plain channel sections and two inside plates as shown in Figs.1 (b) and (d).
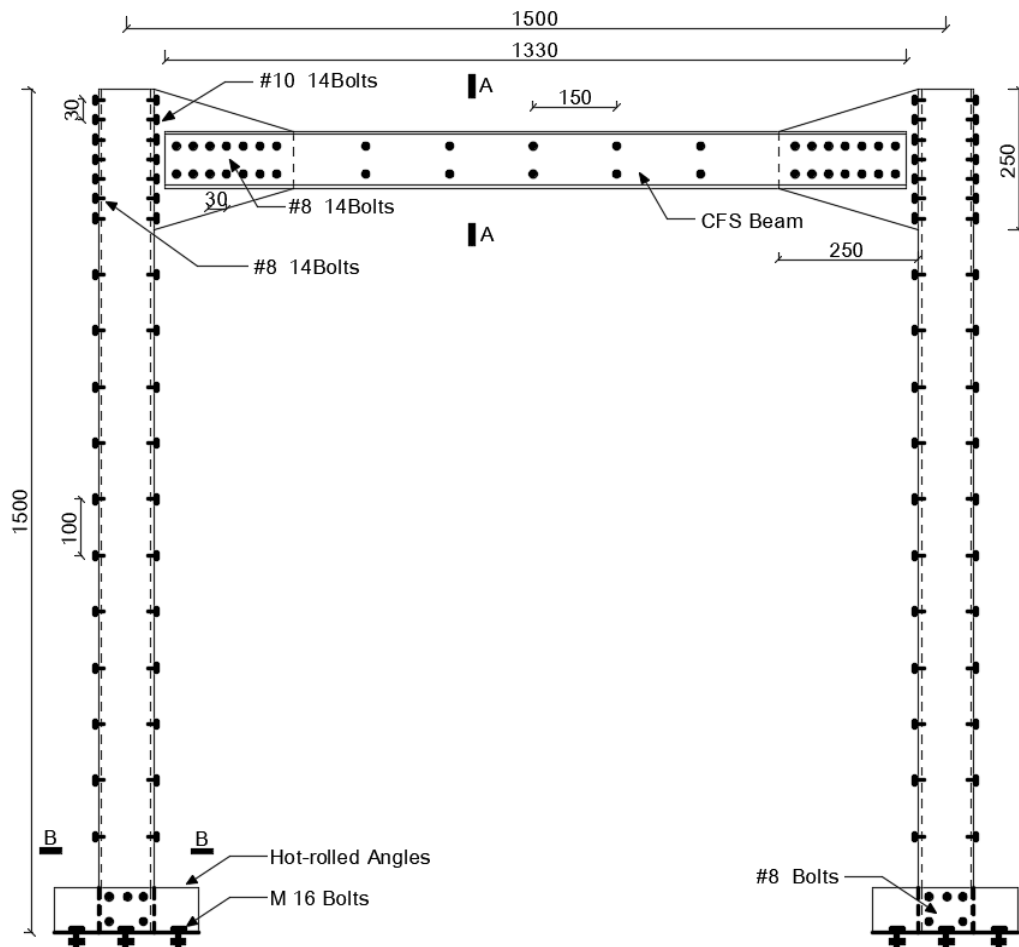
(a) Frame elevation.
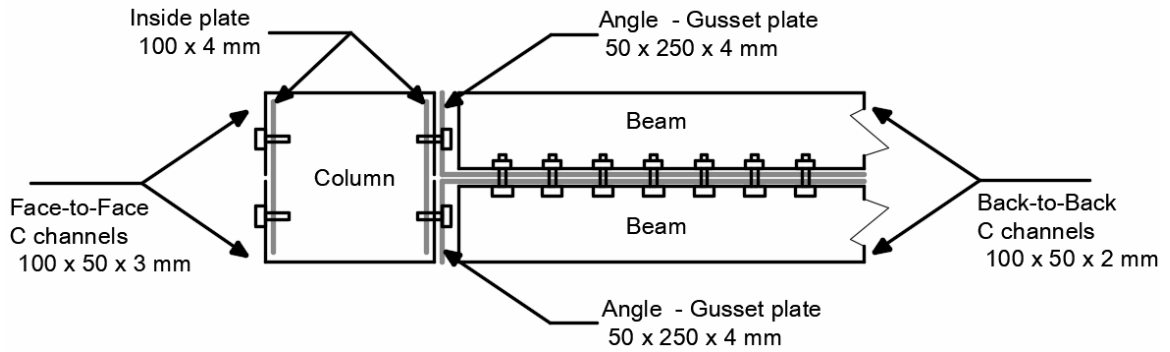
(b) Fabrication of beam to column connection.
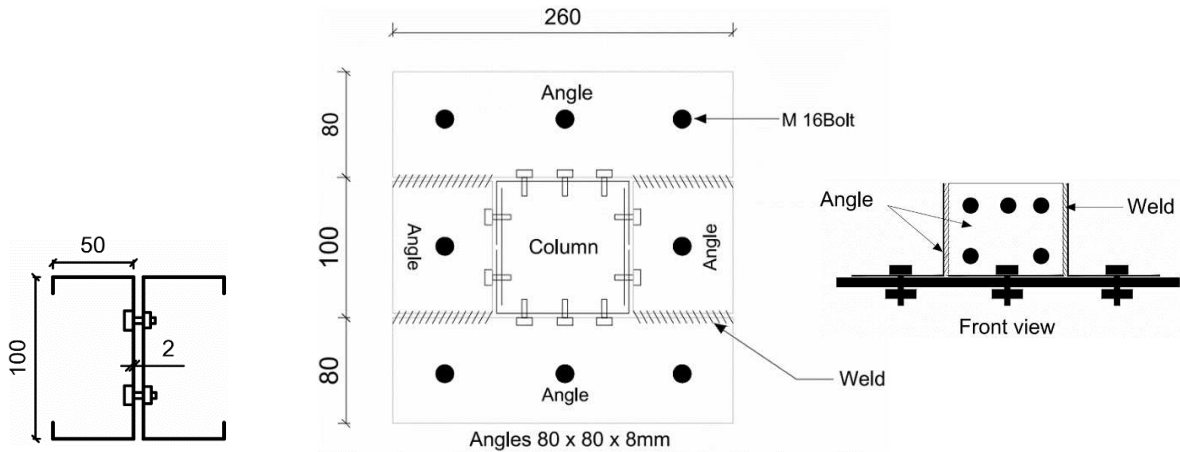
(c) A-A. Beam section.   (d) Column-to-base connection.

Fig. 1. Dimensions and detailing of the tested frame

The general design philosophy adopted was to provide rigid moment resisting connections using a strong column weak beam approach. The box-shaped columns provide a practical design solution for moment-resisting joints in 3D frames. In this study, the inside plates were connected to the channels' flanges by means of #8 bolts as shown in Fig. 1 (a). Using inside plates offered the following advantages: (i) helped the CFS column element act as a unified box section, and (ii) eliminated the need for welding to shape the box-shaped columns, which is especially important considering the low weld-ability of galvanized steel sheets in comparison with normal ST37 steel sheets [17]. It should be noted that welding of CFS sections with low thickness could also cause perforation and damage in the channels.

The steel grade of S275 was used for CFS framing members with the specified minimum yield strength and tensile strength of 275 and 370 MPa, respectively. The beam section consisted of two back-to-back CFS lipped channel sections with the dimensions of 100×50×2 mm and L=1330 mm length. The CFS lipped channels were connected by two rows of #8 bolts as shown in

(c) A-A. Beam section.   (d) Column-to-base connection.

Fig. 1 (c). Two back-to-back angle-shaped sections were used as a gusset plate to transfer vertical forces and bending moments [6, 12]. The gusset plates (250×50×4 mm) were connected to the beam and column elements by using fourteen #8 and #10 bolts (grade 8.8), respectively. Figs. 1 (a) and (b) show the configuration of the beam to column connections in more details. It should be noted that, due to inaccessibility, conventional nuts could not be used inside the box-shaped columns. Thus, the inside plates were threaded at the location of the holes to fix the connection bolts. It should be noted that this type of bolts can provide higher strength compared to the conventional self-tapping screws, which is especially important for moment resisting frame connections in seismic regions. Standard washers were located under the head of all connection bolts and nuts to prevent rotation of the bolts and deformation of the thin material in the vicinity of the bolt holes. The diameter of all bolt holes was fabricated 1 mm larger than the nominal diameter of the bolts.

The column base rigid connections were fabricated using two pairs of hot-rolled angles with dimensions of 80×80×8 mm. The hot-rolled angle sections were bolted to an I-shape base beam by using M16 bolts, grade 8.8. The base beam was then welded to the rigid floor of the laboratory (see Fig. 1 (d)). It was previously shown that using hot-rolled angle cleats for column-to-base bolted connections, in general, can provide high stiffness and rigidity [18]. To

prevent premature failure modes and enhance the capacity of the column-to-base connection, the flanges of the angles were joined by full penetration welding with 10 mm thickness as shown in

(c) A-A. Beam section.   (d) Column-to-base connection.

Fig. 1 (d).

2.2   **Experimental Test Setup**

The experimental test setup used in this study is shown schematically in Fig. 2. A 600 kN hydraulic actuator operating in displacement control was utilised to apply horizontal displacement at the top of the column. A thick steel plate was attached to the end of the hydraulic actuator to prevent premature local damage at the place of loading. Furthermore, to ensure that CFS moment-resisting frame has no out-of-plane deformation and to prevent unexpected instabilities and torsional buckling of the test specimen, a lateral bracing was placed at the end of the beam element as shown in Fig. 3. The contact surfaces between the CFS beam and the lateral bracing system were lubricated to avoid friction.

The test was conducted under displacement control conditions, where the monotonic lateral load was gradually applied to the top of the frame columns until failure occurred. To obtain a quasi-static loading procedure, the load was applied at a gradual rate of 0.1mm/sec to let the structure deform in a ductile manner and also to help identifying local damage in the structural elements and connections.

It should be noticed that that the CFS moment resisting frame would experience some stiffness and strength degradation under cyclic loading, which cannot be captured by the static monotonic tests conducted in this study. However, cyclic loading tests on CFS moment resisting connections indicated that this degradation is not significant if the plate thickness is

more than 3 mm, even when the local elastic buckling occurs before yielding of the cross-section [11].
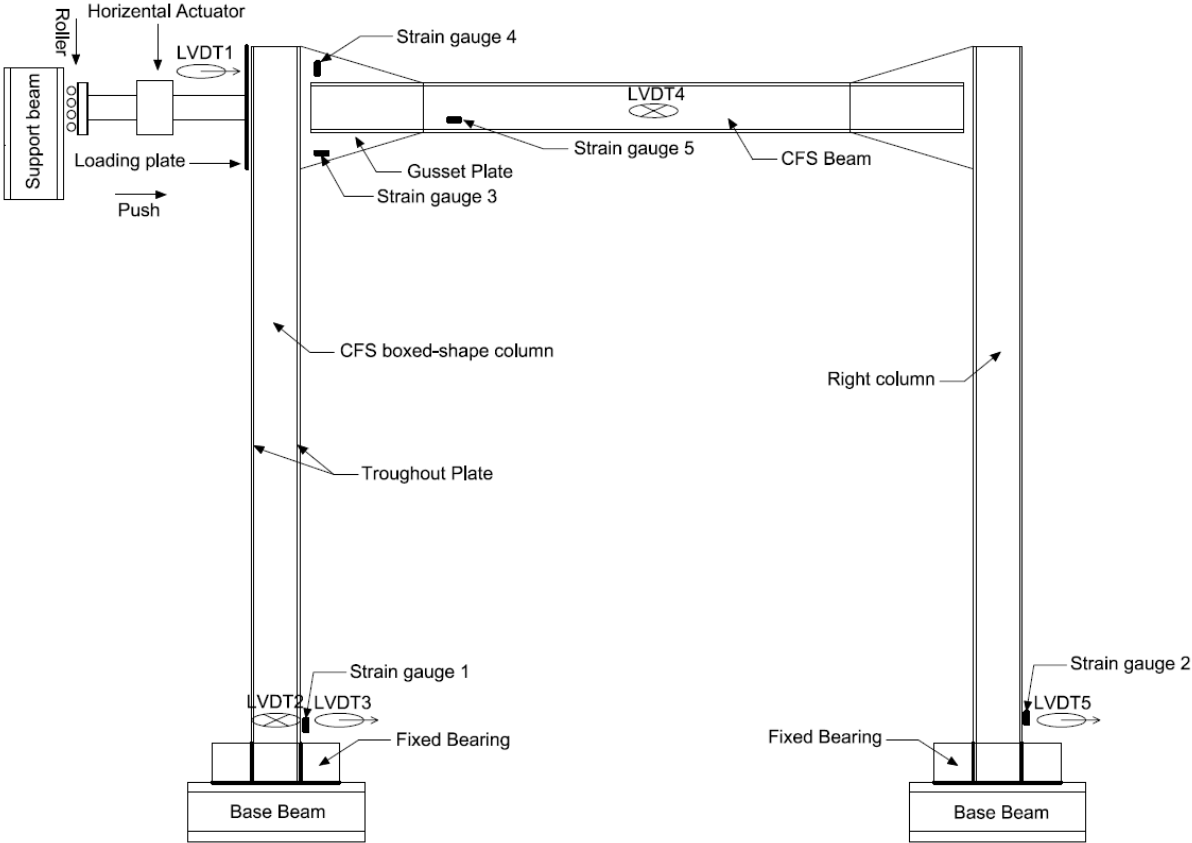
Fig. 2. Experimental test setup
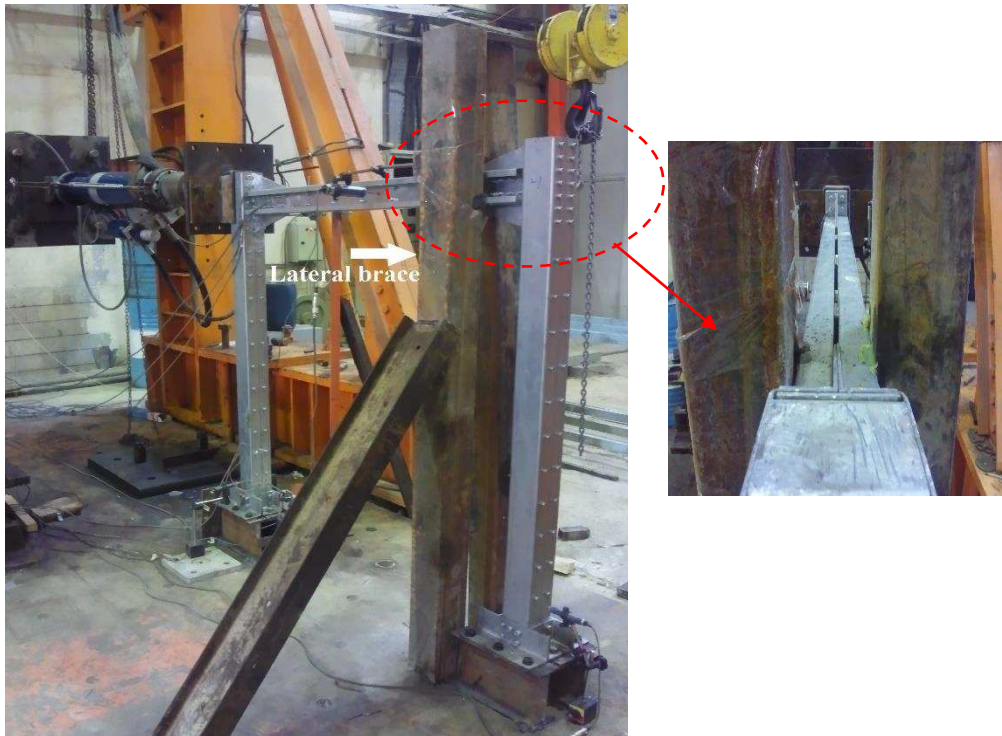
Fig. 3. Lateral bracing of the frame

The applied lateral load and the lateral displacements were recorded by using a load cell and a displacement transducer (LVDT1) attached to the hydraulic actuator (to verify the lateral displacement obtained from the actuator). Another four LVDTs (no. 2, 3, 4, 5) were used to measure deformations at the selected points on the beam and column elements where premature local damage was expected to occur. In addition, five strain gauges were used to measure the strains at the beam web, column flange and the expected locations of plastic hinges within gusset plates. Fig. 2 shows the locations of the strain gauges and LVDT displacement transducers. All LVDTs and strain gauges were connected to a multi-channel data logger and the digital readings of the load, displacement and strains were recorded in each load step.

2.3   **Material properties**

All CFS elements used in the moment-resisting frame were formed from same steel plate. To measure the material properties of the CFS specimens, three coupon tensile tests

were conducted according to ASTM A370 [19]. The yield stress (0.2% proof stress), ultimate stress, fracture strain and the module of elasticity measured for the tested coupons are given in Table 1.

Table 1. Material properties obtained from experiments

	Test number			
	1	2	3	Ave
0.2% proof stress (MPa)	325	311	303	313
F_{max} (UTS) (MPa)	401	381	364	382
Strain at fracture	22.1%	21.3%	18.8	20.7%
Thickness (mm)	1.04	1.02	0.98	1.01
E-Modulus (GPa)	210	207	204	207

The average of the measured yield stress, Young's modulus and ultimate stress values were used to calculate the critical buckling load of the channel sections and evaluate the lateral load capacity of the frame. As mentioned before, high strength M16 bolts (ISO grade 8.8) were employed to connect the CFS column to the base beam by using four angles (Fig. 1 (d)). No material tests were carried out for bolts and hot-rolled angles, as their strength was inferred to be less critical than the strength of the channels. Based on the standard specification for heat-treated steel structural bolts [20], the grade 8.8 bolts were hand tightened with a wrench and had a minimum tensile strength of Fu=800 MPa (120/105 ksi Minimum Tensile Strength) [20]. The nominal yield stress of the hot-rolled angles provided by the manufacturer was 350 MPa.

2.4 Experimental test results

The lateral load was gradually applied at the top of the left column of the CFS moment-resisting frame. Fig. 4 shows the location of the local damages observed during the

experimental test. The first indication of damage was observed at the bottom of the right column in the compressive side close to the column-to-base connection (Fig. 5(a)), shortly followed by the damage at the bottom of the left column. Subsequently, the top of both CFS columns at the locations close to the gusset plate connection exhibited local failures (Fig. 5(b)). At this stage, outward deformations were observed in the channel web, while the inside plates, channels' flanges and gusset plates all exhibited inward deformations. As shown in Fig. 5, the half-wave length of the dominant local buckling mode was around 30 mm and 120 mm with inward displacements at the bottom and the top of the columns, respectively. The frame was ultimately reached a failure mechanism due to four local failures located at the top and the bottom of the columns as shown in Fig. 4. The main reason for the dominant failure mode observed in the experimental test is the fact that no vertical load was applied to the CFS beam element. This can represent a structural system were the gravity loads are only applied to the columns (e.g. by using one way slabs). While due to the limitations of the available laboratory equipment, the vertical loads were not applied to the CFS columns, the effect of the column axial loads on the overall seismic behaviour of the frame was investigated by validated FE models (see Section 4).

As discussed before, in the experimental test set-up the base was significantly stiffened by using strong angles at the column-to-base connections. While the joint rotational stiffness was not measured directly in this study, no clear opening up of the angles on the tension side and closing of the angles on the compression side was observed at the base after the experimental tests. This may indicate that the base connections were adequately rigid, and explain why the failure points were shifted from the base angles to the bottom of the columns.

At the end of the experimental test, none of the column-to-base connection angles experienced any bolt bearing deformation around the bolt holes. In addition, there were no

shear failure and pull-out in the bolts connecting the components of the CFS beam and column elements.
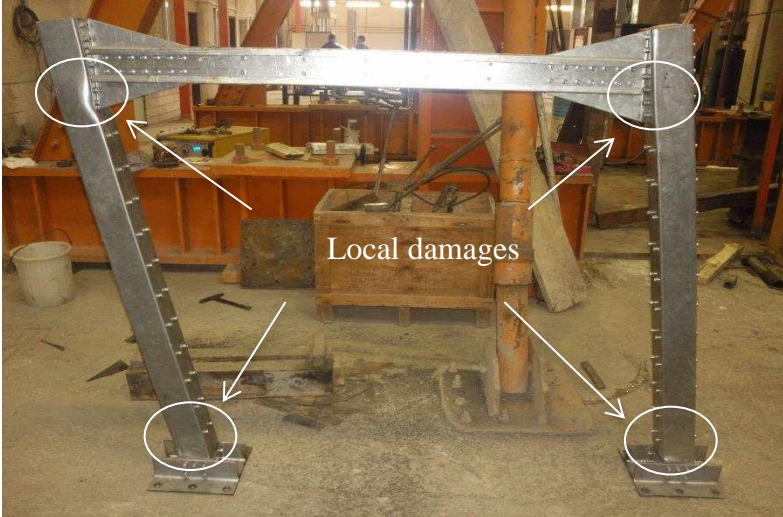
Fig. 4. Permanent deformations and local damages observed at the ultimate point

(a)　　　　　　　　　　　　　　　　(b)

Fig. 5. Local damage observed at the (a) the bottom of the CFS columns and (b) top

Fig. 6 shows the lateral load (P) versus lateral displacement (Δ) curve of the tested CFS moment resisting frame. The performance of the frame is studied in four different phases (A to D) as identified in Fig. 6. The first phase (0-A) corresponds to the elastic state, in which the frame was pushed up to 86 mm (5.7% drift ratio) applying a lateral load of 38.14 kN (the maximum lateral load capacity of the frame). The second phase (A-B), started with the buckling of the plate components at the bottom of the right column shortly followed by the

buckling at the bottom of the left column. These local damages created a softening branch in the load-displacement curve of the CFS frame showing a considerable strength and stiffness degradation. During the development of the softening branch, the bottom of the deformed columns became in contact with the angles used in the column-to-base connection, which eventually led to an increase in the post-buckling lateral load capacity of the frame. In the third phase (B-C), the frame was pushed up to 250 mm until reaching the nominal failure point (Point C). During this Phase, local damage at the top of both CFS columns (close to the column-to-gusset plate connections) was observed at the lateral force of 37.45 kN. As a result, the lateral stiffness of the frame became very small at 250 mm lateral displacement (Point C), where a collapse mechanism was practically developed. In the final phase (C-D), the frame was pushed up to the capacity of hydraulic actuator (300 mm). The local damages at the top of the columns progressively increased and gradually involved the web of the channel sections (see Fig. 5 (b)). The experimental test was stopped at this stage.
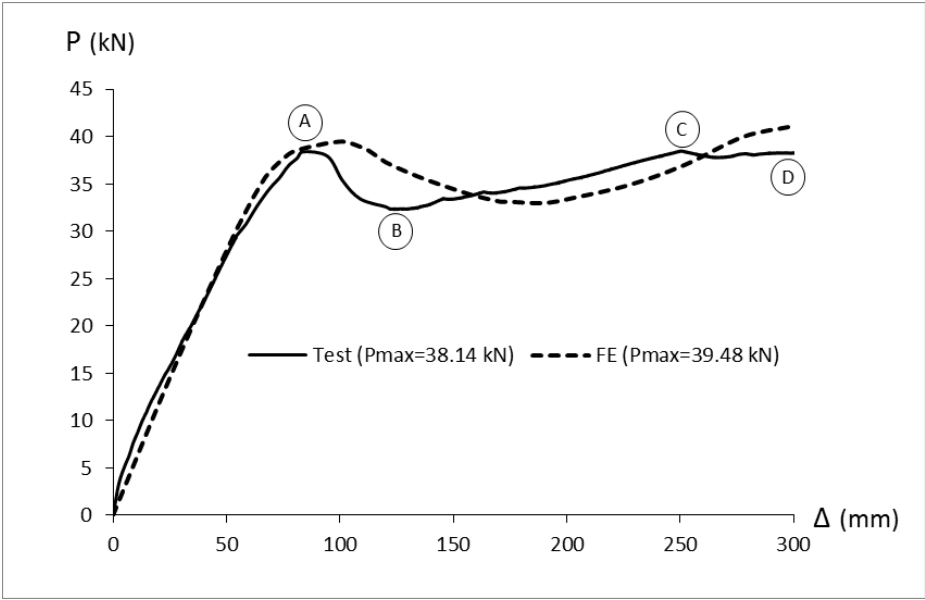
Fig. 6. Lateral load versus lateral displacement curves obtained from experimental test and detailed FE model.

Fig. 7 compares the maximum compressive strain values extracted from the strain gauges installed on the five selected locations shown in Fig. 2, normalised by the proof strain

$\varepsilon_y = 0.2\%$. The results indicate that no material yielding occurred at the beam, column or gusset plate elements until the failure point. The strain values for the CFS box-shaped columns (strain gauges 1 and 2) increased uniformly up to the beginning of the web crippling or local damage (Point A), while a significant drop was observed after buckling occurred. The CFS beam element showed a similar behaviour (strain gauge5); however, the drop in the strain-displacement curve was considerably less significant. The horizontal and vertical strains in the gusset plates (strain gauges 3 and 4) in general were very small. The main reason is that these elements (back-to-back 50×250×4 mm angles in Fig. 1(b) were designed to be significantly more rigid than the adjacent elements of the frame.
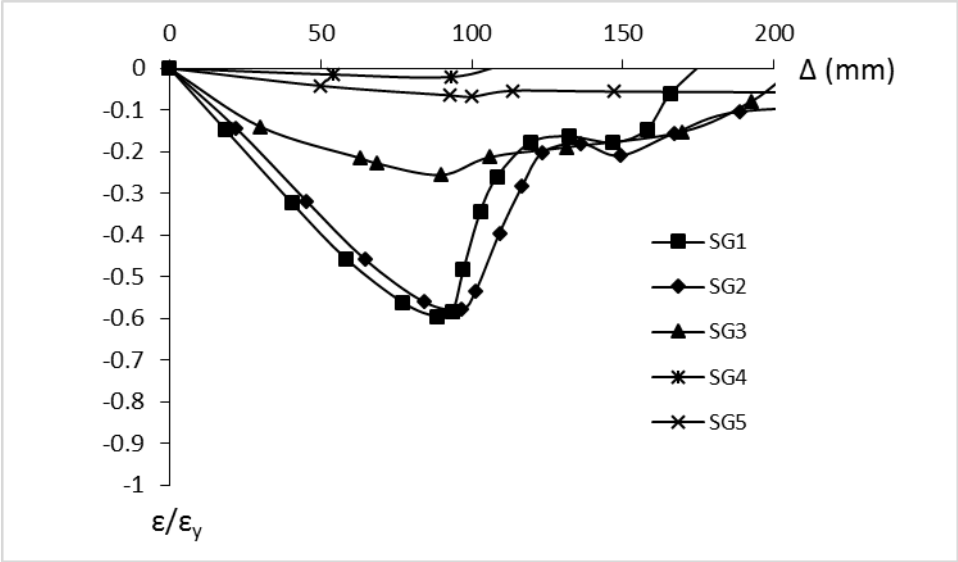
Fig. 7. Normalised strains (ε/ εy) versus lateral displacement at the selected locations

3 FINITE ELEMENT MODELLING

A detailed FE model was developed using FE package ABAQUS [21] to simulate the structural performance of the tested CFS moment-resisting frame under lateral loads. The developed model takes into account the effects of geometrical imperfections and material nonlinearity and is validated based on the experimental results discussed in the previous sections.

3.1   **Element type and material properties**

To represent the accurate behaviour of the tested CFS moment-resisting frame, the main components of the frame were modelled including: column channels, beam channels, inside plates, angle-shaped gusset plates, base plate angles and bolts. A 4-node non-linear shell element with reduced integration points (to reduce the computational cost) was used to model all plate elements. It was found that a mesh size of 15×15 mm provides accurate results while does not significantly increase the computational time. Fig. 8 shows the developed FE model and the boundary conditions.
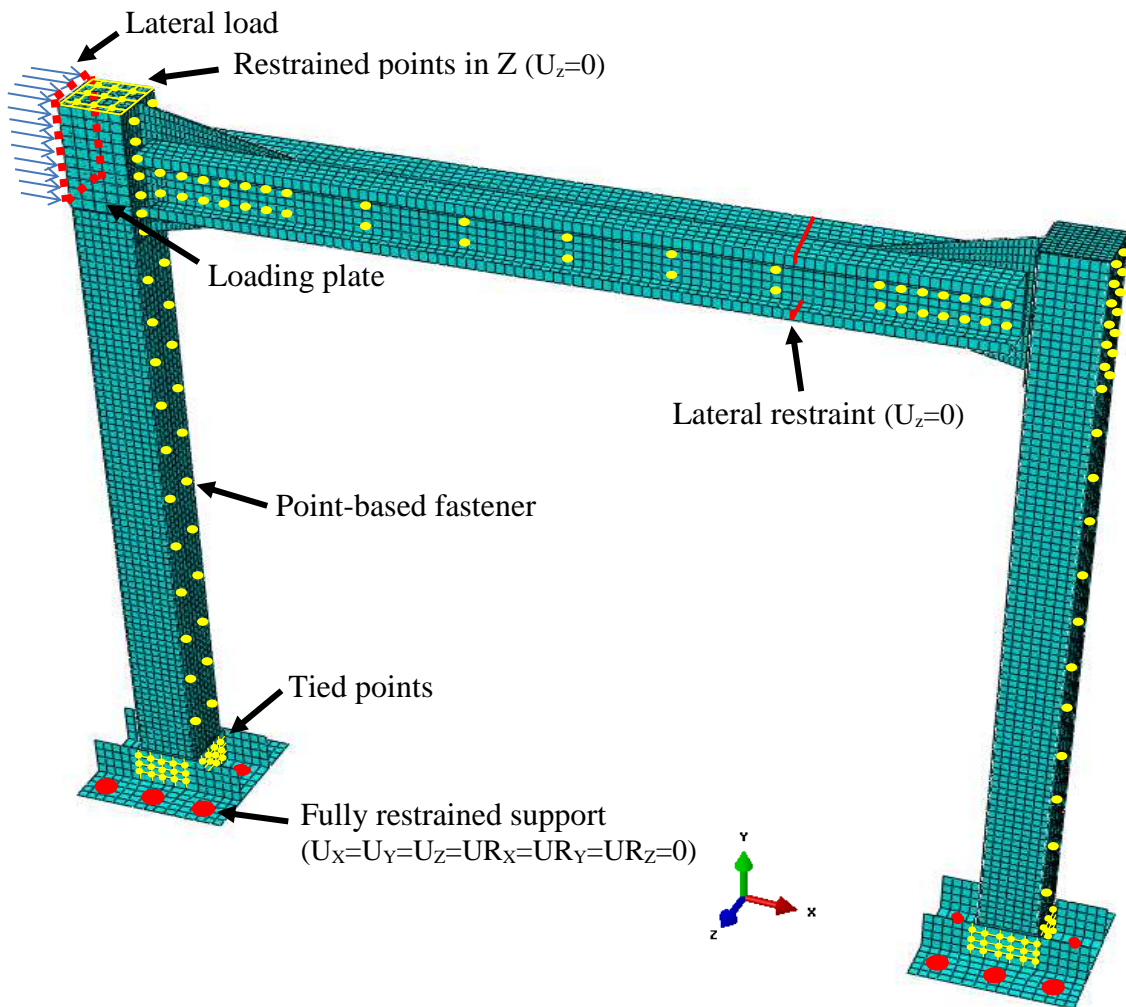

Fig. 8. Typical finite element model of the tested CFS moment-resisting frame.

Fig.9 illustrates the tress-strain relationship used in the FE analyses, which is a simplified material model adopted from Haidarali and Nethercot [22, 23]. Based on this method, the stress strain curve is composed of the basic Ramberg-Osgood stress-strain relationship up to the 0.2% proof stress, followed by a straight line with a slope of E/100. This model has previously proved to yield realistic results when compared to the experimental tests on the distortional buckling of CFS members performed by Yu and Schafer [24]. Mathematically, the stress–strain model is expressed as:

$$\varepsilon = \frac{\sigma}{E} + 0.002 \left(\frac{\sigma}{\sigma_{0.2}} \right)^{n} \qquad \text{for } \sigma \le \sigma_{0.2}$$

$$\varepsilon = \varepsilon_{0.2} + \frac{100(\sigma - \sigma_{0.2})}{E} \qquad \text{for } \sigma \ge \sigma_{0.2}$$

$$(1)$$

where $\sigma_{0.2} = 313\text{MPa}$ and $E = 207\text{GPa}$ are the average of the measured 0.2% proof stress and modulus of elasticity of the CFS material obtained from coupon tests (see Table 1). $\varepsilon_{0.2}$ is defined as the strain corresponding to the 0.2% proof stress. The parameter n of the Ramberg-Osgood model determine the stress-strain curve shape giving the best fit to the results of the coupon tests. It is herein taken as 10 as suggested by Rasmussen [25].
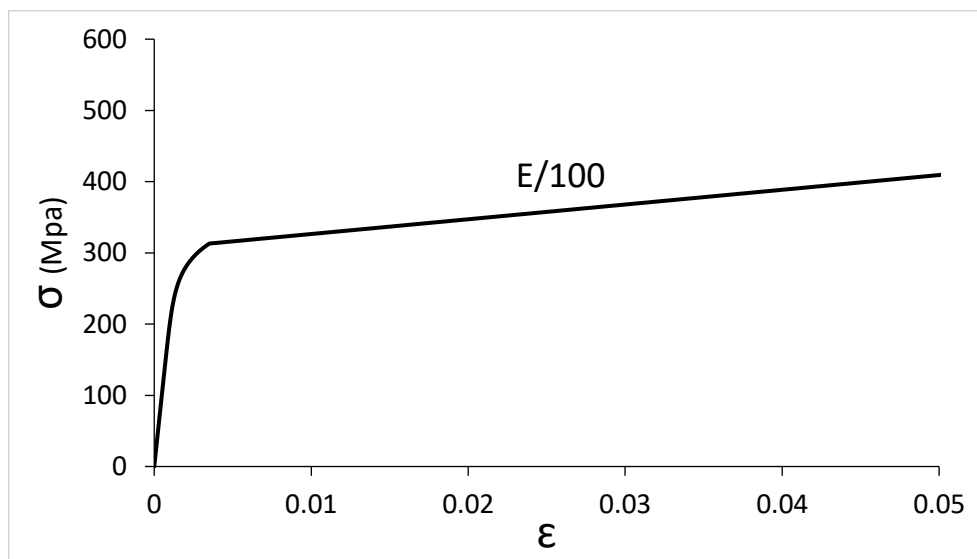
Fig. 9. Stress-strain relationship used in the FE analysis.

3.2   Geometrical imperfections

The cross-sectional shapes of the CFS beam and column channels were generated by taking into account geometrical imperfections using an eigenvalue elastic buckling analysis in ABAQUS [21]. The first buckling mode of the frame was used to find the general shape of the local and distortional imperfections. The calculated geometrical imperfections were then scaled and superimposed to obtain the initial state of the CFS frame. The scale factors were defined as $0.34t$ and $0.94t$ for the local and distortional imperfections, respectively, as proposed by Schafer and Peköz [26] for the sections with thickness (t) less than 3mm. Depending on which mode provided the lowest critical buckling resistance, local or distortional imperfections were incorporated into the model. The effects of membrane residual stress were not included in the FE model as previous studies showed they can be safely neglected in open sections [27].

3.3   Bolt modelling

The point-based "fastener" element in ABAQUS [21] was employed to model the bolt groups in the FE models. Beam and column elements were connected to gusset plates by a series of fasteners located at the position of the bolts and connector elements were used to define the interaction between the CFS elements which are connected by fasteners. As it was mentioned before, no slippage was observed in the bolts during the experimental test. Therefore, to prevent bolt slippage, translational and rotational degrees of freedom for each pair of fastener point were coupled by using the "BEAM" connector element in ABAQUS [21]. In addition, a physical radius (r) equal to the half of the bolt shank diameter was assigned to each fastener. The displacement and rotation of each fastener point were then considered as average of the nearby nodes. Using this modelling approach could prevent stress concentrations around the bolt position in the FE model and improve the convergence of the analyses.

3.4 **Loading and boundary conditions**

Since a very thick loading plate was used in the experimental test, no deformation was observed in the plate at the end of the tests. Therefore, to simulate the loading condition a discrete rigid shell element was used to model the loading plate (Fig. 8). The base angles at the location of the bolts were also fully constrained by using "Tie" command in ABAQUS [21]. In order to model the lateral bracing used in the experimental test (Fig. 3), the out-of-plane displacements of the beam channel lips were restrained at the location of the lateral bracing as shown in Fig. 8.

3.5 **Validation of the FE results**

The presented experimental test results were used to validate the developed nonlinear FE model. Nonlinear inelastic analysis (pushover) was performed using the standard "Static General" arc-length method in ABAQUS, where the stiffness degradation due to the buckling of the CFS elements was taken into consideration.

Fig. 6 compares the lateral monotonic load (P) versus lateral displacement (Δ) results obtained from the experimental test and detailed FE models. In general, it is shown that the FE results compare well with the experimental observations over the whole loading range. The slight differences between the analytical and the experimental results in the initial elastic stage can be attributed to the small friction in the lubricated interface of the beam and bracing elements. While the analytical results could simulate the post-buckling stiffness degradation of the frame with a good accuracy, they do not show the zero stiffness at the failure point C. The main reason can be attributed to the additional strength provided by the fixed bearing connections in the FE models. However, this minor difference does not affect the overall accuracy of the analytical results. It is shown in Fig. 6 that the developed FE model could

predict the maximum lateral load capacity of the CFS frame with less than 5% error (FE model: 39.48 kN, Experiment: 38.14 kN). Similar to the experimental observations, the first indication of local failure in the FE model occurred at the bottom of the CFS columns in the same lateral displacement (Point A in Fig. 6), which was followed by the local failure at the top of the columns.

Fig. 10 illustrates the von Mises stress distribution and the failure mode of the analysed CFS frame. It is shown that the developed FE model could efficiently capture four local damages similar to the tested frame at the beam-to-column and column-to-base connections.

It should be noted that while no experimental tests under axial loads were conducted on the reference CFS frame, as a part of this research study, the detailed FE models for CFS columns under axial loads and the nonlinear cyclic response of the CFS bolted moment resisting connections were validated against experimental tests conducted at the University of Sheffield [28, 29]
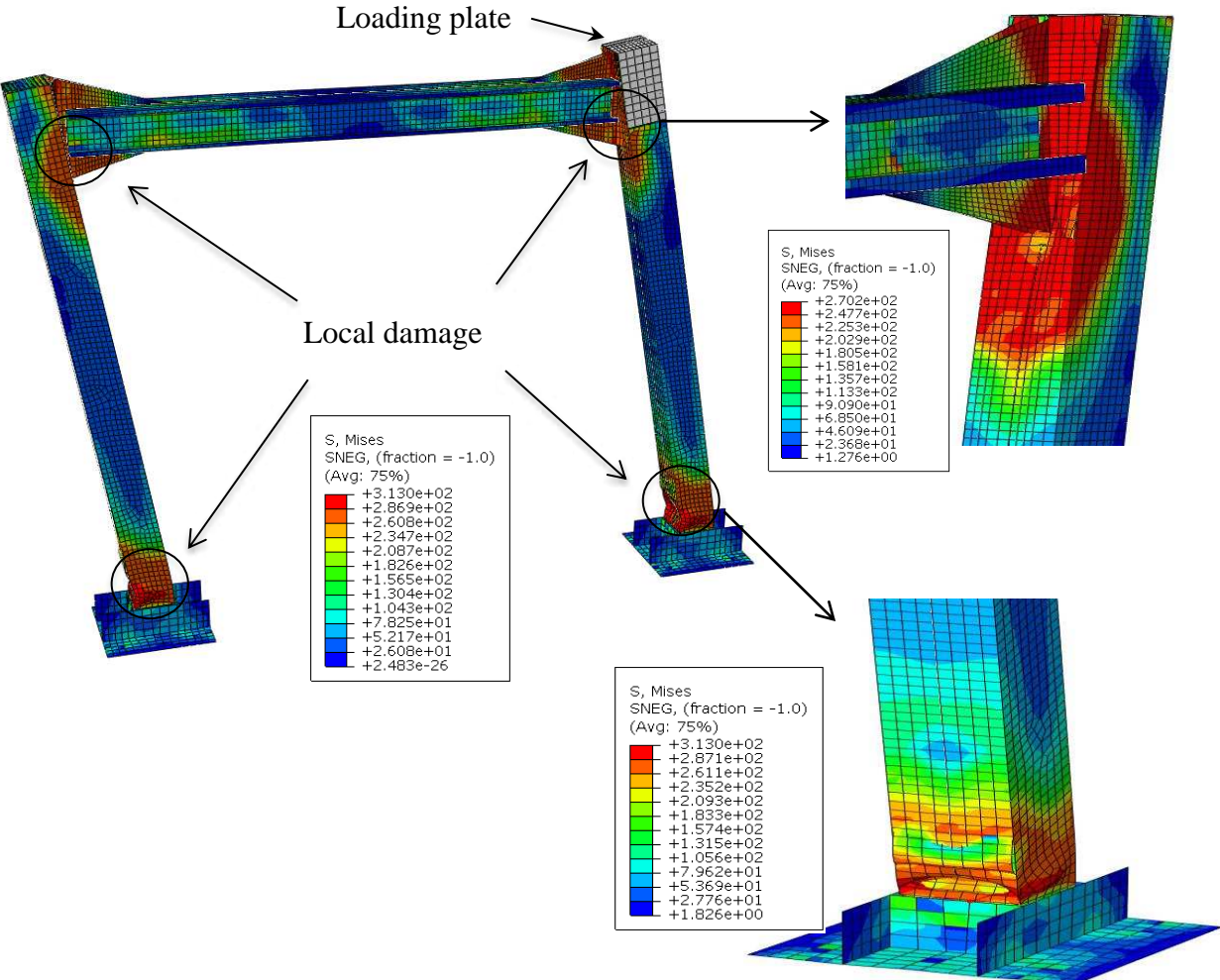
Fig. 10. von-Mises stress distribution and the failure mode of the CFS frame

4 PARAMETRIC STUDY

In accordance with the AISC 341-16 [30], moment resisting frames are categorised into three different groups based on their ductility, including Special Moment Frames (SMFs), Intermediate Moment Frames (IMFs), and Ordinary Moment Frames (OMFs). While SMFs should be capable of incorporating 4% or more inter-storey drift angle with maximum 20% strength degradation, IMFs and OMFs are designed to accommodate between 2% and 4%, and less than 2% inter-storey drift angle, respectively. On the other hand, based on AISC [30] requirements for steel buildings in seismic regions (seismically compact), the width-to-thickness ratios of box-shaped columns for moderately ductile and highly ductile members are limited to $b/t \leq 0.64\sqrt{E/f_y}$ and $b/t \leq 0.55\sqrt{E/f_y}$, respectively, where b, t, E, and f_y are the width, thickness, module of elasticity and yield stress of the column. For low ductile members, there is no limit on the b/t ratio.

Based on the validated FE model developed in Section 3, a comprehensive parametric study is conducted to provide insight into the lateral capacity, energy dissipation capacity, and ductility of CFS moment resisting frames with box-shaped columns. Nine CFS moment-resisting frames were designed using different column axial loads and cross-sectional width-to-thickness ratios as key design parameters influencing the seismic behaviour of MRFs. The column axial load ratio is defined as $n = N_0/N_u$, where N_0 is the applied axial load to the column and N_u is the axial compressive capacity of the box column which is calculated based on the buckling resistance of the compression member proposed by AISI S-100 [7]. Three

levels of column axial load ratios $n = 0.05, 0.2, 0.5$, and also three columns with different width-to-thickness ratios $b/t = 20, 14.3, 10$ were considered (nine different frames in total).
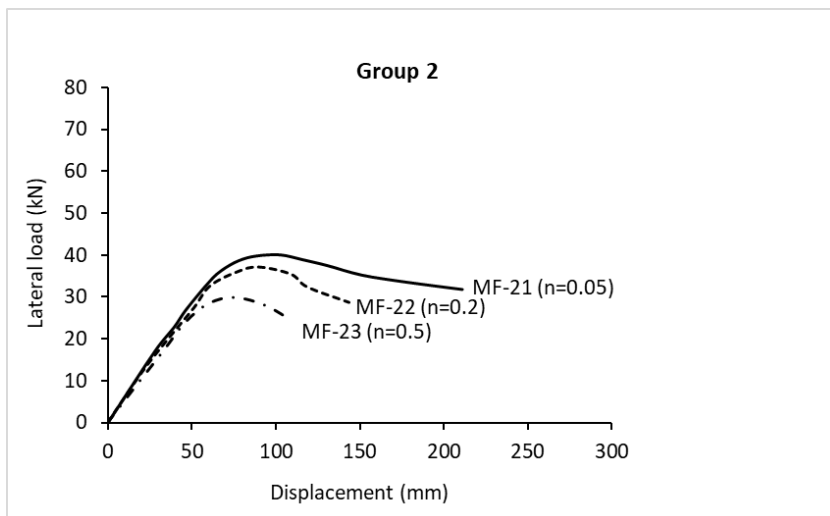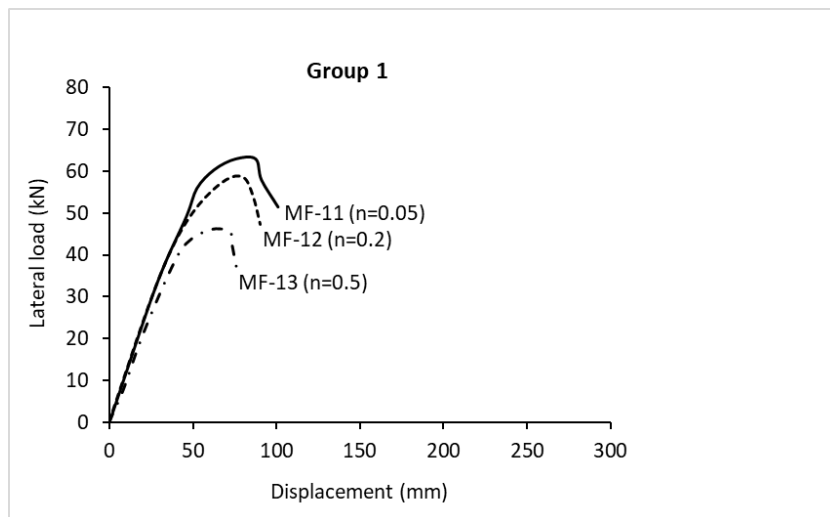
Table 2 lists the dimensions of the box-shaped columns with various width-to-thickness ratios b/t and back-to-back beam channels used in each MRF, as well as the considered axial loads N_0 and axial load ratios n. The frame size, diameter of the bolts used in different locations, distance of the bolts along the length of the CFS beam and column elements, and the dimension of the base angles were kept the same as the tested frame. The element type, mesh size, material properties, geometrical imperfections, modelling of the bolts, boundary conditions and loading protocol were also consistent with those mentioned in Section 3. The gravity loads and P-D effects were considered in the pushover analysis conducted in ABAQUS [21]. To provide a better comparison, the frames were categorised in three different groups based on the width-to-thickness ratio of their columns (see Table 2).

Fig. 11 shows the lateral load (P) versus lateral displacement (Δ) curves for the three groups of the CFS moment resisting frames. The frames were pushed laterally until reaching the failure point, which is defined as 20% reduction from peak lateral load of the lateral load response curve [30]. It should be mentioned that, similar to the reference experimental test, the typical failure mode of all studied frames was due to the local damage (web-crippling) at the top of the columns at the location of beam-to-column connections and bottom of the columns close to column-to-base connections (see Fig. 12). The seismic characteristics of the MRFs including their lateral load and displacement capacity, energy dissipation, ductility, and ductility reduction factor are investigated in the following sections.

Table 2. Summary of frame specimen information

Specimen Number	Specimen size (mm)		N_0 (kN)	n
	Column ▢	Beam ⊐⊏		

|	Section size	Thickness (t)		Width-to-thickness ratio b/t	Length	Lipped-channel size	Thickness (t)	Length		
		Plain Channel	Inside plate							
MF-11	140×140	3	4	20	1500	140×70×20	3	1500	18	0.05
MF-12	140×140	3	4	20	1500	140×70×20	3	1500	72	0.2
MF-13	140×140	3	4	20	1500	100×50×20	2	1500	181	0.5
MF-21	100×100	3	4	14.3	1500	120×60×20	3	1500	13	0.05
MF-22	100×100	3	4	14.3	1500	120×60×20	3	1500	52	0.2
MF-23	100×100	3	4	14.3	1500	100×50×20	2	1500	129	0.5
MF-31	100×100	4	6	10	1500	120×60×20	4	1500	18	0.05
MF-32	100×100	4	6	10	1500	120×60×20	4	1500	72	0.2
MF-33	100×100	4	6	10	1500	100×50×20	3	1500	179	0.5

Group 1 — Lateral load (kN) vs Displacement (mm): MF-11 (n=0.05), MF-12 (n=0.2), MF-13 (n=0.5)

Group 2 — Lateral load (kN) vs Displacement (mm): MF-21 (n=0.05), MF-22 (n=0.2), MF-23 (n=0.5)
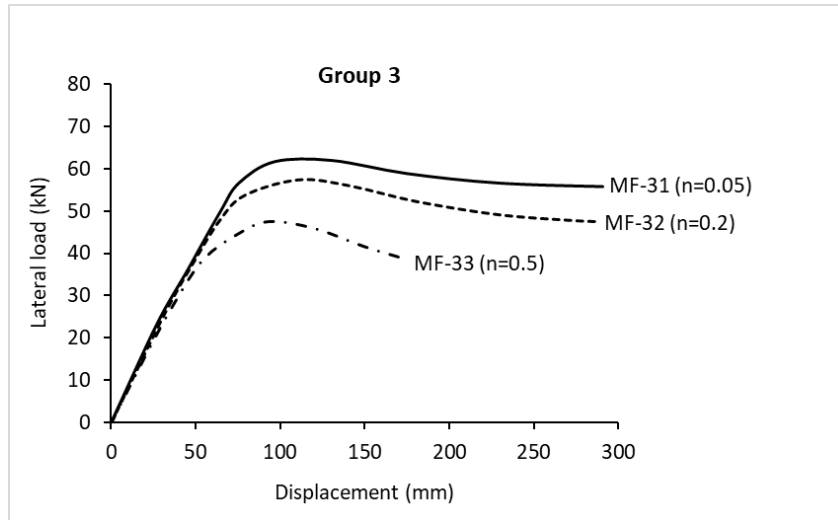
Fig. 11. Lateral load (P) versus lateral displacement (Δ) curves obtained from FE models of the three groups of MRFs.
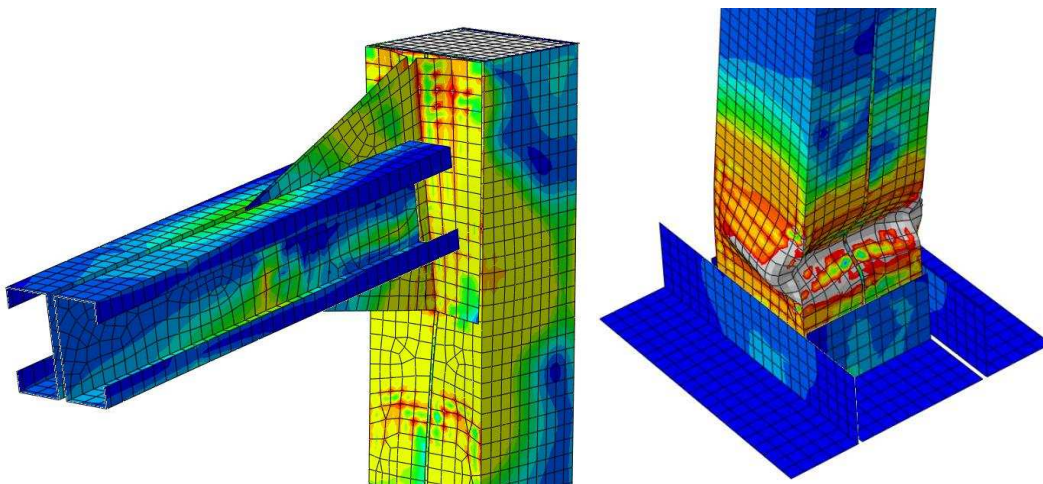
Fig. 12. Typical failure mode of the studied frames, local damage at (a) top and (b) bottom of the CFS columns.

4.1 Monotonic vs. cyclic loading

To investigate the differences between the response of the reference moment-resisting frame under lateral monotonic and cyclic loading, the CUREE cyclic loading protocol (ASTM E2126–1 [31]) was applied on the detailed FE model in ABAQUS [21] using the University of Sheffield's High Performance Computing (HPC) cluster. Fig. 13 compares the behaviour of the frame under the monotonic and the cyclic loading. It is shown that the

system exhibits slightly higher strength and stiffness degradations under the cyclic loading condition. However, the results indicated that the response of the frame under monotonic loading provides a reasonable representative of the cyclic loading envelop curve. Therefore, it was decided to use the results of the monotonic loads to determine the seismic performance of the frames in this study. This can considerably simplify the analytical calculations, since performing cyclic analyses on a detailed CFS frame model in ABAQUS [21] is very computationally expensive due to the large number of nonlinear shell and surface to surface contact elements and fasteners.
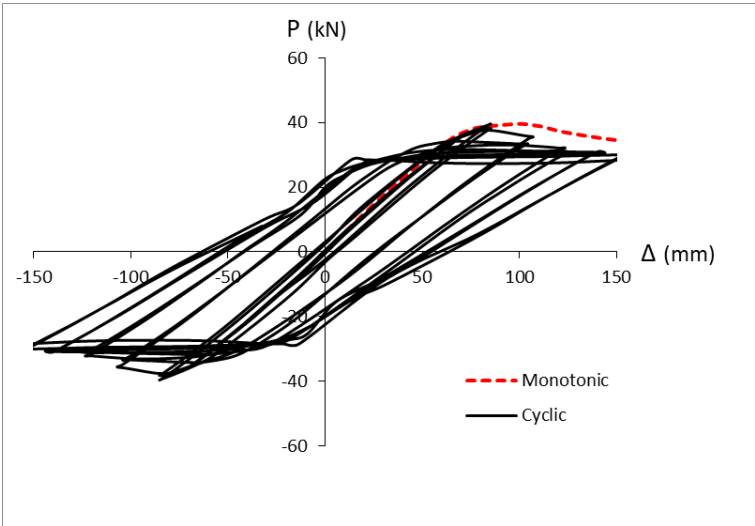
Fig. 13. Comparison between the response of the reference moment-resisting frame under lateral monotonic and cyclic loading

4.2 **Lateral load and displacement capacity**

Fig. 14 illustrates the maximum lateral load capacity of the frames listed in Table 2. While the MRFs in Group 2 had lower lateral load capacities, the load capacity of the MRFs in Groups 1 and 2 were relatively close. The results indicate that by increasing the axial load ratio n, the lateral load capacity in each group of MRFs decreases at a similar rate. By imposing an axial load on the columns up to 20% and 50% of the compressive capacity of the

columns (i.e. n= 0.2 and 0.5), the lateral capacity of the MRFs decreased on average by 10% and 26%, respectively. This reduction in the lateral load capacity can be explained by the fact that the buckling of the column web is intensified by the presence of axial load in combination with localized forces due to the frame action.

The results in Fig. 14 also indicate that the selected MRFs with CFS box-shaped columns in general were capable to provide adequate lateral deformation capacity to satisfy the SMF requirements of AISC 341-16 [30]. It should be noted that while the frames in Group 1 suffer from brittle failure leading to significant drop in the softening stage of the lateral load-displacement curve, their initial elastic stage can accommodate the 4% inter-storey drift required for SMFs. However, these elements will exhibit a very low ductility as will be discussed in Section 4.3.
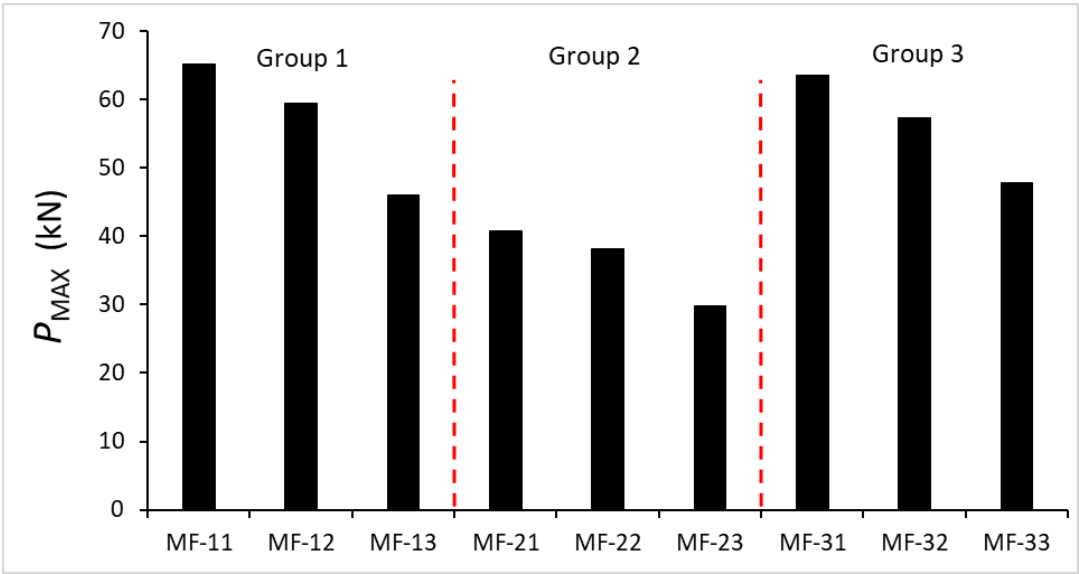

Fig. 14. Maximum lateral load capacity of different MRFs obtained from FE models

4.3   **Energy dissipation**

One of the key seismic performance parameters is the ability of the structures to absorb the energy of the input earthquake (P_E). In CFS frames, P_E can be calculated based on the area

under the lateral load–displacement curve until the post-peak lateral load of the system drops by 20% (i.e. nominal failure point). Fig. 15 compares the energy dissipation capacity of the different MRFs obtained from FE models. It can be seen that the energy dissipation capacity of the CFS frames under lateral seismic loads always decreases by increasing the axial load ratio (n). This behaviour is especially evident in M-33, where increasing the axial load resulted in a failure at the bottom of the columns at considerably lower lateral displacements compared to M-31 and M-32 (see Fig. 11). Increasing the axial load to 20% and 50% of the axial capacity of the columns, reduced the energy abortion capacity of the frames by 24% and 53% in Group 1, 39% and 62% in Group 2, and 22% and 65% in Group 3, respectively.

The results in Fig. 15 also indicate that, for the same axial load ratio, the energy dissipation capacity of the CFS frames in Group 3 (with lower b/t ratios) is considerably higher than the other groups. This implies that b/t ratio is a key parameter in providing higher energy dissipation capacity in CFS frames.
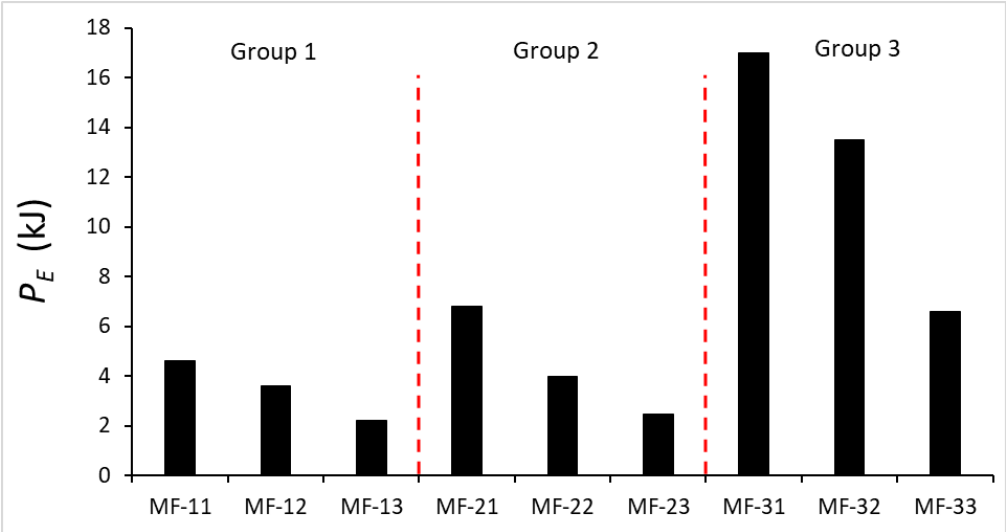

Fig. 15. Comparison of energy dissipation capacity of different MRFs obtained from FE models.

4.4   Ductility Ratio

Ductility is defined as the ability of the structure to undergo plastic deformations without significant loss of strength, which is especially important in controlling the structural damage during strong earthquakes. The ductility ratio of the CFS moment-resisting frames can be determined using the following equation:

$$\mu = \frac{\Delta_u}{\Delta_y} \qquad\qquad (2)$$

where Δ_y and Δ_u are the yield and the ultimate displacement of the frame, respectively. In this study, the yield displacement was determined based on ASCE/SEI 41-13 [32] (and FEMA 356 [33]) recommended method, where the load-displacement curve is represented by a bilinear curve with a post-yield slope as shown in Fig. 16. The yield displacement (Δ_y) is determined on the condition that the secant slope intersects the actual envelope curve at 60% of the nominal yield force (P_y), while the area enclosed by the bilinear curve is equal to that enclosed by the original curve bounded by the target displacement (Δ_t). The target displacement was assumed to be corresponding to the displacement at which the lateral load capacity of the system dropped by 20% (i.e. $\Delta_t = \Delta_u$).
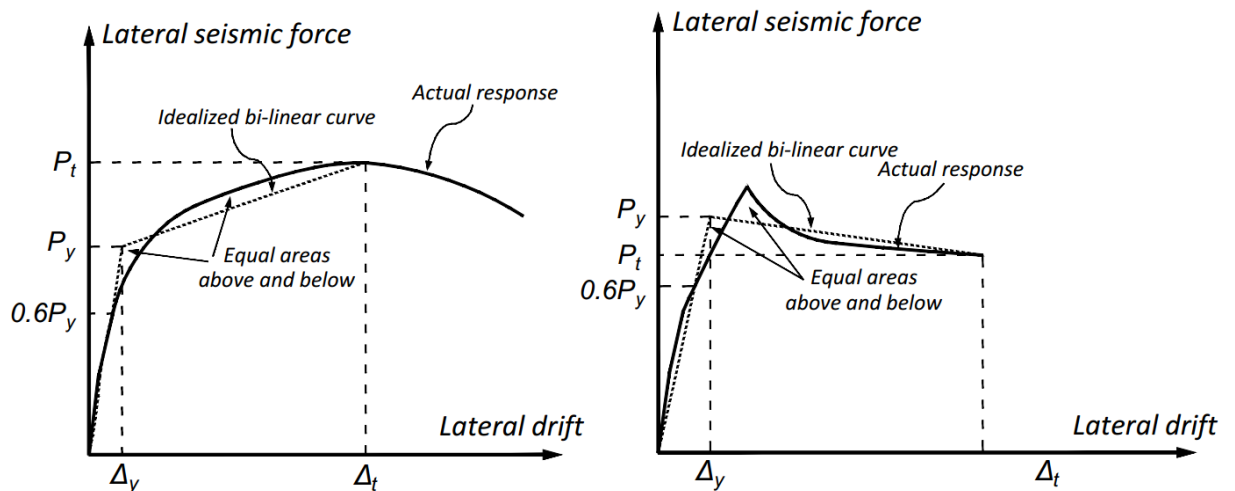
(a) Positive post-yield slope   (b) Negative post-yield slope

Fig. 16. Definition of the yield and target displacements for calculation of ductility.

Table 3 lists the calculated yield displacements and ductility ratio of the different MRFs. The results indicate that by decreasing the width-to-thickness ratio of the box-shaped columns, the ductility ratio of the frames increases. This is more evident for the frames with lower axial load ratios (i.e. n=0.05), where the frames in Group 3 exhibited 155% and 65% higher ductility ratios compared to the Group 1 and Group 2 counterparts. Increasing the axial load ratio from 0.05 to 0.5, however, decreased the ductility ratio of the frames by up to 20%, 42% and 51% in Groups 1, 2 and 3, respectively.

Table 3. Estimated yield displacement, fundamental period, ductility, and ductility reduction factor for different MRFs.

Specimen	Δ_y (mm)	T (sec)	$R_\mu = \mu$
MF-11	45.2	0.65	2.2
MF-12	45.1	0.65	1.9
MF-13	39.4	0.6	1.8
MF-21	59.6	0.89	3.5
MF-22	60.2	0.89	2.5
MF-23	57.7	0.84	2.1
MF-31	65.9	0.85	5.6
MF-32	65.5	0.85	4.5
MF-33	63.3	0.81	2.9

4.5   **Ductility Reduction Factor**

While conventional design methodologies are usually based on the elastic behaviour of structural elements, typical structures have the capacity to exhibit nonlinear deformations and dissipate hysteretic energy under strong earthquakes. In the seismic design of structures, the

behaviour factor, R, is usually used to reduce the seismic load effects to the strength level as specified by the applicable building code. In general, the R factor consists of three different parameters as given by the following equation [34]:

$$R = R_S R_\mu R_R \qquad (3)$$

where, R_S is the over-strength factor, R_μ is the ductility reduction factor and R_R is known as the redundancy factor to account for the number and distribution of active plastic hinges. The ductility reduction factor (R_μ) is mainly used to reduce the elastic design force obtained from an elastic design spectrum to the yield strength level (P_y) [35, 36]. Based on the Newmark and Hall method [37], the ductility reduction factor (R_μ) can be considered as a function of the ductility ratio (μ) and the fundamental period (T) of the structure. Table 3 compares the fundamental period (T) of the designed CFS frames, estimated by using the Finite Element Frequency analysis available in ABAQUS library [21]. Since the T values for all CFS frames are greater than 0.5 sec, according to the Newmark and Hall proposed equations [37], the ductility reduction factor (R_μ) would be equal to the ductility ratio μ (see Table 3).

According to FEMA 450 [35], the required ductility reduction factors R_μ are recommended to be over 5.5, 4, and 3 for SMF, IMF, OMF, respectively. Therefore, the results in Table 3 imply that the CFS frames in Group 1 and 2 cannot be used as an OMF seismic resistant system, except for the case with a very low axial load ratio in Group 2 (MF-21). However, the ductility reduction factor for the CFS frames in Group 3 with low (MF-31) and moderate (MF-32) axial load ratios were 5.6 and 4.5, which satisfy the requirements of SMF and IMF, respectively. It is worth mentioning that all nine CFS MRFs were able to accommodate over 4% inter-storey drift ratios that is one of the requirements for SMFs in AISC 341-16 [30] as discussed in section 4.1. Hence, the key parameter for the seismic design

of CFS MRFs seems to be the ductility reduction factor R_μ, which is shown to be mainly affected by the width-to-thickness ratio of the plate components constituting the CFS cross-sections and the axial load ratio of the columns.

The results of this study, in general, show the seismic performance and limitations of the CFS MRFs in seismic regions and should prove useful in practical applications for more efficient design of CFS structural systems.

5 SUMMARY AND CONCLUSIONS

This paper aimed to investigate the seismic behaviour of an innovative cold-formed steel (CFS) moment-resisting portal frame using box-shaped columns. An experimental test was conducted on a half-scale CFS moment-resisting frame, and the nonlinear seismic performance of the frame was investigated in detail. The experimental results were then used to validate detailed FE models in ABAQUS by taking into account the material non-linearity, geometrical imperfections and the effects of bolts. The FE models could predict the ultimate strength and failure mode of the reference frame accurately and compared well with the experimental observations over the whole loading range. To evaluate the structural behaviour of the proposed CFS moment-resisting frame system, a comprehensive parametric was then conducted using various axial load levels and CFS plate components width-to-thickness ratios. The effects of these design parameters on the lateral load capacity, ultimate displacement, energy dissipation, ductility, and ductility reduction factor were investigated. Based on the results presented in this paper, the following conclusions can be drawn:

(1) The experimental results show that the proposed CFS moment-resisting frame system can provide high lateral load resistance suitable for seismic applications. The first indication of damage was observed at the bottom of the columns in the compressive side close to the

column-to-base connections. Subsequently, the top of the CFS columns close to the gusset plate connections exhibited local damage due to buckling of the plates and the frame ultimately reached a failure mechanism. The strain readings from the experimental test indicated that no material yielding occurred at the beam, column and gusset plate elements up to the buckling point (point A in Fig. 6). However, in the post buckling phase (B-D) plastic deformations were clearly observed at the location of the web crippling (or local damage) at the bottom of the CFS columns.

(2) By increasing the axial load to 50% of the axial compressive capacity of the CFS columns, the ultimate lateral load, the energy dissipation capacity, and the ductility ratio of the CFS moment-resisting frame decreased by up to 26%, 62%, and 50%, respectively. In general, these reductions are more significant for the MRFs with high cross-sectional width-to-thickness ratios.

(3) The energy dissipation capacity and ductility ratio of the MRF increased significantly (up to 300% and 155%, respectively) by decreasing the width-to-thickness ratio of the columns. However, the lateral load capacity was more affected by the size of the columns rather than the width-to-thickness ratio of the plate components.

(4) All designed MRFs have the adequate lateral sway capacity of 4% inter-storey drift required for SMFs in AISC 341-16 [30]. However, the parametric study demonstrated that CFS frames in Groups 1 and 2 (i.e. b/t≥ 14) usually do not satisfy the OMF seismic resistant system criteria in accordance with FEMA 450 [35] due to the premature buckling of the columns leading to low ductility. The ductility reduction factor for CFS frames of Group 3 (i.e. b/t≤10) with low and moderate axial load ratios were 5.6 and 4.4, which satisfy the requirements of SMF and IMF recommended by FEMA 450 [35], respectively.

REFERENCES

[1] B.W. Schafer, D. Ayhan, J. Leng, P. Liu, D. Padilla-Llano, K.D. Peterman, M. Stehman, S.G. Buonopane, M. Eatherton, R. Madsen, B. Manley, C.D. Moen, N. Nakata, C. Rogers, C. Yu, Seismic Response and Engineering of Cold-formed Steel Framed Buildings, Structures, 8, Part 2 (2016) 197-212.

[2] D. Dubina, Behavior and performance of cold-formed steel-framed houses under seismic action, Journal of Constructional Steel Research, 64 (2008) 896-913.

[3] H. Moghimi, H.R. Ronagh, Performance of light-gauge cold-formed steel strap-braced stud walls subjected to cyclic loading, Engineering Structures, 31 (2009) 69-83.

[4] L. Fiorino, O. Iuorio, R. Landolfo, Designing CFS structures: The new school bfs in naples, Thin Wall Structures, 78 (2014) 37-47.

[5] J.B.P. Lim, D.A. Nethercot, Finite element idealization of a cold-formed steel portal frame, Journal of Structural Engineering, 130 (2004) 78-94.

[6] J.B.P. Lim, D.A. Nethercot, Ultimate strength of bolted moment-connections between cold-formed steel members, Thin Wall Structures, 41 ((2003)) 1019-1039.

[7] American Iron and Steel Institute (AISI), North American specification for the design of cold-formed steel structural members, 2012 [AISI S100-12].

[8] J.B.P. Lim, G.J. Hancock, G.C. Clifton, C.H. Pham, R. Das, DSM for ultimate strength of bolted moment-connections between cold-formed steel channel members, Journal of Constructional Steel Research, 117 (2016) 196-203.

[9] A. Sato, C.-M. Uang, Seismic design procedure development for cold-formed steel–special bolted moment frames, Journal of Constructional Steel Research, 65 (2009) 860-868.

[10] American Iron and Steel Institute (AISI), Standard for seismic design of cold-formed steel structural systems-special bolted moment frames; 2007 [AISI S110-2007].

[11] A. Bagheri Sabbagh, M. Petkovski, K. Pilakoutas, R. Mirghaderi, Experimental work on cold-formed steel elements for earthquake resilient moment frame buildings, Engineering Structures, 42 (2012) 371-386.

[12] W.K. Yu, K.F. Chung, M.F. Wong, Analysis of bolted moment connections in cold-formed steel beam–column sub-frames, Journal of Constructional Steel Research, 61 (2005) 1332-1352.

[13] Ž. Bučmys, A. Daniūnas, Analytical and experimental investigation of cold-formed steel beam-to-column bolted gusset-plate joints, Journal of Civil Engineering and Management, 21 (2015) 1061-1069.

[14] A. Wrzesien, J.B.P. Lim, D.A. Nethercot, Optimum joint detailed for a general cold-formed steel portal frame. Advances in Structural Engineering 2012; 15(9):1635-1651.

[15] American Iron and Steel Institute (AISI), North American Standard for seismic Design of Cold-Formed Steel Structural Systems, 2015 [AISI S400-15].

[16] A.B. Sabbagh, R. Mirghaderi, M. Petkovski, K. Pilakoutas, An integrated thin-walled steel skeleton structure (two full scale tests), Journal of Constructional Steel Research, 66 (2010) 470-479.

[17] American Welding Society's specification D-19.0, Welding Zinc Coated Steel. AWS;2005.

[18] M. Dundu, Base connections of single cold-formed steel portal frames, Journal of Constructional Steel Research, 78 (2012) 38-44.

[19] ASTM A370, Standard Testing Methods and Definitions for Mechanical Testing of Steel Products, 2014 Edition.

[20] ASTM, A325, Specification for structural joints using American Institute of Steel Construction. Chicago, Illinois, (2004).

[21] Abaqus/CAE User's Manual, 2007, version 6.7, USA.

[22] M.R. Haidarali, D.A. Nethercot, Finite element modelling of cold-formed steel beams under local buckling or combined local/distortional buckling, Thin Wall Structures, 49 (2011) 1554-1562.

[23] W. Ramberg, W.R. Osgood, Description of stress-strain curves by three parameters. , Technical note no. 902. Washington, DC: National Advisory Committee for Aeronautics; 1943.

[24] C. Yu, B.W. Schafer, Distortional Buckling Tests on Cold-Formed Steel Beams, Journal of Structural Engineering, 132 (2006) 515-528.

[25] K.J.R. Rasmussen, Full-range stress–strain curves for stainless steel alloys, J Constr Steel Res 1(2003) 47–61.

[26] B.W. Schafer, T. Pekoz, Computational modeling of cold-formed steel: characterizing geometric imperfections and residual stresses, J Constr Steel Res, 47 (1998) 193-210.

[27] B.W. Schafer, Z. Li, C.D. Moen, Computational modeling of cold-formed steel, Thin-Walled Structures, 48 (2010) 752-762.

[28] W. Ma, J. Becque, I. Hajirasouliha, J. Ye, Cross-sectional optimization of cold-formed steel channels to Eurocode 3, Engineering Structures, 101 (2015) 641-651.

[29] J. Ye, More efficient cold-formed steel elements and bolted connections, PhD thesis, University of Sheffield; 2016.

[30] ANSI/AISC, 341-16, Seismic provisions for structural steel buildings, american institute of steel construction (AISC), (2016).

[31] American Iron and Steel Institute. North American standard for cold-formed steel framing lateral design. 2007 Ed. AISI S213-07; 2007.

[32] ASCE/SEI, 41-13, Seismic Rehabilitation of Existing Buildings, (1st Edition), American Society of Civil Engineers (ASCE), (2013).

[33] FEMA-356. Pre standard and commentary for the seismic rehabilitation of buildings. USA, Virginia: American Society Of Civil Engineers; 2000.

[34] B. Borzi, A.S. Elnashai, Refined force reduction factors for seismic design, Engineering Structures, 22 (2000) 1244-1260.

[35] FEMA-450. NEHRP recommended provisions for seismic regulations for new buildings and other structures—part1: provisions. USA: Building Seismic Safety Council; 2003.

[36] C.M. Uang, Establishing R (or Rw) and Cd factors for building seismic provisions, Journal of Structural Engineering, 117(1) (1991) 19–28.

[37] Newmark NM, Hall WJ. Earthquake spectra and design. California,USA: Earthquake Engineering Research Institute, Berkeley; 1982.